Nanoscale Focused Ion Beam from Laser-Cooled Lithium Atoms

B Knuffman[1], A V Steele[1], J Orloff[2] and J J McClelland[1]

[1]Center for Nanoscale Sciences and Technology, National Institute of Standards and Technology, Gaithersburg, MD 20899 USA

[2]FEI Company, Hillsboro, Oregon 97124 USA

E-mail: jabez.mcclelland@nist.gov

Abstract. We demonstrate a new type of nanoscale focused ion beam (FIB) based on photoionizing laser-cooled atoms held at millikelvin temperatures in a magneto-optical trap (MOT). This new source expands the range of available ionic species and accessible ion beam energies for FIBs, enhancing their role as one of the most important tools for nanoscale characterization and fabrication. We show examples of microscopy with lithium ions obtained by scanning the FIB and collecting the resulting secondary electrons, and characterize the beam focus by a 25% to 75% rise distance measurement of (26.7 ± 1.0) nm at a beam energy of 2 keV. We also examine the dependence of the focal size on MOT temperature and beam energy.

Keywords. Focused ion beams; ion microscopy; laser cooling; lithium ions; ion sources

PACS: 07.78+s, 37.10.Gh, 37.10.De, 41.75.Ak, 79.90.+b

Submitted to New Journal of Physics

Focused ion beams (FIBs) are an invaluable tool for the fabrication and characterization of materials with nanoscale feature sizes. FIBs add or remove material to create or modify nanostructures through sputtering or through beam-activated chemistry with a precursor gas [1]. Ion microscopy offers higher surface sensitivity and distinct contrast mechanisms when compared with scanning electron microscopy [2]. FIBs also enable spatially resolved elemental analysis using secondary ion mass spectrometry (SIMS) [3]. However, existing FIB technology is limited to relatively few ionic species that can be focused to the nanometer scale. Additionally, such focusing typically requires beam energies of 10 keV or more because of inherent energy spread in the ion beam. Operating over a wider range of ionic species and beam energies would enable a host of new nanofabrication and nanoanalysis tools.

In this paper we report on the creation of a FIB system based on a magneto-optical trap ion source (MOTIS) [4] that makes use of the ultracold temperatures achievable with laser cooling. We have realized a lithium ion microscope capable of focusing low-energy (< 2 keV) lithium ions to form a nanoscale probe and scanning the focused beam to acquire secondary electron images. We have characterized the size of the focus and have investigated the beam size as a function of both the temperature of the atoms and beam energy. This work demonstrates an entirely new approach to creating a nanoscale FIB; this approach opens possibilities for FIBs composed of a variety of ionic species and has a particular advantage for high resolution at low beam energies.

The MOTIS has recently been investigated [4] as a source that offers significant advantages over existing technologies such as the widely-used liquid metal ion source (LMIS) [2], the gas field ionization source [5], or plasma sources [6]. In principle, any atom that can be laser-cooled is compatible with MOTIS technology, enabling the creation of isotopically pure ion beams from alkalis, alkaline earths, noble gases, and several metals – over 20 different species in all [7]. The choice of species can be tailored to the application. For example, a light ion is well-suited for microscopy because of its low sputter yield, avoiding sample damage that can limit imaging resolution [8]. Alternatively, a heavy ion with relatively high sputter yield is desirable for milling applications. Moreover, choosing an ion with specific chemical properties can greatly enhance applications such as beam chemistry or SIMS analysis [9].

At low beam energies (below a few thousand electron volts), sputtering, implantation of contaminants during milling, and damage created during chemically assisted etching and deposition [1] are all reduced. Also, with energies below 1 keV, direct deposition of material becomes possible [10]. However, obtaining a nanoscale focal spot at low energy is typically hampered by chromatic aberrations in the focusing lens arising from longitudinal energy spread in the ion beam. The energy spread in a MOTIS - due to the creation of ions over a finite spatial extent in a nonzero electric field - can be made very small (< 100 meV) compared with that of the LMIS ($\approx$ 5 eV), making is especially suited to low energy applications.

A number of theoretical analyses of the MOTIS and similar sources have been performed that describe how low-emittance, high-brightness, and low-energy-spread charged particle beams can be created from laser-cooled atoms [4,11,12]. Measurements of Cr MOTIS emittance [13] have shown that it can be as small as 6×10^{-7} mm mrad $(\text{MeV})^{1/2}$, a value competitive with the LMIS, and formation of a rudimentary Cr FIB has been recently reported [7]. Measurements of the energy spread of ion bunches from a pulsed rubidium MOTIS report values as low as 0.02 eV [14], two orders of magnitude lower than typical values for the LMIS. Other experimental and theoretical work has identified both the deleterious effects of stochastic Coulomb interactions on emittance and brightness and areas of operational parameter space where such effects are manageable [15,16].

For the present demonstration we have chosen Li^+ as an ion of particular interest for a number of reasons. Li is a relatively light element, and so we expect it to be well suited to microscopy with minimal sample damage from sputtering. On the other hand, Li^+ tends to have a high mobility and prefers interstitial sites in materials like silicon [17], suggesting it may have a sample interaction that is very different from a light noble gas ion such as He^+. In addition, Li^+ is known to have a much higher backscattering probability than He^+ [18], suggesting that it could be useful for surface sensitive, enhanced contrast imaging at low impact energy. A further benefit is the relative simplicity of the laser system required for laser cooling.

Our FIB system consists of a Li MOTIS integrated with a conventional ion optical column and is shown in Fig. 1. The ion beam is created by photoionizing laser-cooled ^{7}Li atoms in a magneto-optical trap (MOT) in an electric field E produced by a voltage difference maintained

across a parallel pair of planar electrodes. The upper electrode is an optical flat coated with a transparent conductor (indium tin oxide). The lower electrode is an aluminum-coated silicon wafer (100 μm thick) with a 4 mm hole to allow the ion beam to pass. The lower electrode serves as a mirror to reflect the MOT beams (see Fig. 1), which are tuned to the 671 nm laser cooling transition in Li. The MOT is loaded using a Zeeman slower (not shown) [19]. The quadrupole MOT magnetic field has a gradient of 0.46 T/m (0.23 T/m) along (transverse to) this axis. We note that the ions are accelerated through the magnetic field gradient by electric fields large enough that beam-distorting effects are negligible. Under typical operating conditions, the MOT has a size (one standard deviation) $\sigma_{\mathrm{MOT}} = 250\ \mu\mathrm{m}$, a load rate of 2 x 10^8 s^{-1}, a typical steady-state population (without ionization) of 2 x 10^7 atoms, and temperatures ranging from 350 μK to 1600 μK.

The ionization laser beam, produced by a frequency-doubled, continuous wave Ti:sapphire laser, is focused through the MOT as shown in Fig. 2 and tuned to 349.9 nm such that atoms in the $2P_{3/2}$ upper state of the laser-cooling transition are photoionized to form $^7Li^+$. The ionization region, defined by the intersection of the MOT with the ionization laser beam, has an elliptical Gaussian focus with characteristic dimensions (one standard deviation) along (transverse to) the ion beam axis of $\sigma_z = 5\ \mu\mathrm{m}$ ($\sigma_y = 20\ \mu\mathrm{m}$). A small σ_z contributes to a proportionately small energy spread in the resultant ion beam. Along the ionization laser beam, the ionization region has a characteristic dimension of σ_{MOT} since the Rayleigh range of the focus is larger than the diameter of the MOT.

After exiting the ionization region, the beam enters a resistive acceleration tube, designed such that the potential drops linearly along the inside of the tube for a fixed voltage difference across the ends of the tube. By distributing the acceleration of the ion beam over the length of the tube, a smaller electric field E is required in the source region to achieve a given final beam energy. Additionally, by tuning the electric fields between the electrode pair and inside the resistive acceleration tube, a weak lens can be formed to control the size and convergence or divergence of the beam delivered to the ion column. The energy spread, which can be expressed as $\sigma_U = e\sigma_z E$, where e is the electronic charge, can be calculated using typical values from our FIB system ($\sigma_z = 5\ \mu\mathrm{m}$ and $E = 14$ keV/m) as $\sigma_U = 70$ meV.

After the beam exits the acceleration tube (held at ground potential), it enters a commercial ion optical column [2]. The first element is a 150 μm diameter aperture. The beam is typically allowed to expand in the accelerating tube such that the short transverse extent of the beam ($\sigma_y = 20\ \mu$m at the source) approximately matches the radius of the aperture. The beam profile is essentially circular after the aperture, ensuring that spherical and chromatic aberrations in the focusing lens do not cause the focal spot to be out of round. Voltages applied to deflector elements allow for beam scanning on the target and correction of astigmatism in the focusing lens. The ion beam is then focused on the target by an einzel lens operated in deceleration mode.

Fig. 2 shows a secondary electron image obtained by scanning a 2 keV $^7Li^+$ ion beam on a target of tin spheres on carbon. The current in the ion beam was 1 pA, and the 885 x 1024 pixel image was acquired in 220 s at a working distance of 10 mm. This image clearly demonstrates the feasibility of using laser-cooled atoms as a focused ion beam source for imaging applications. We note that, as expected for a light ion, no appreciable sputtering of the target was observed during the image acquisition.

To characterize the focal spot size, we measured the rise distance of the secondary electron signal as the beam was scanned across the edge of a cleaved $\langle 100 \rangle$ silicon wafer tilted at a 5° angle with respect to the incident beam. Images of the knife edge were formed line by line with the ion beam scanned in a direction normal to the edge, as seen in Fig. 3(a). An error function was fit to the image intensity data of the edge for each line. The rise distance for each line was defined to be the distance over which the error function fit rose from 25 % to 75 % of the difference between its maximum and minimum values (see sample line scan in Fig. 3(b)). The measured rise distance $d_{25/75}$ was defined to be the average of the rise distance over all 850 lines in the image. Random error from counting statistics on individual line scans adds much less than 1 % uncertainty to the average value [20].

The following sources of systematic uncertainty are important to consider. First, the magnification of the acquired image must be calibrated to enable the conversion of image pixels to distance. This calibration has an uncertainty of ± 2 %. Second, the relative sharpness of the knife edge was examined using scanning electron microscope images showing a rise distance of 3 nm, possibly limited by the size of the electron beam focus. In any case, the width of the

convolution of a 3 nm edge with a 27 nm ion beam would reflect the width of the ion beam to greater than 99 % accuracy.

Nine repeated measurements of the rise distance under the operating conditions yielding the best recorded beam size are shown in Fig. 3(c). Between each measurement, the astigmatism correction was re-optimized, and the ion beam was refocused; this minimized the effects of electronic drift and allowed us to gauge the random error associated with the tuning of critical ion optical elements. From these measurements, we determine the rise distance to be $d_{25/75} = (26.7 \pm 1.0)$ nm. The beam had an energy of 1915 eV and contained a current of 0.7 pA at the sample.

For a MOTIS with a Gaussian spatial distribution and angular distribution arising from thermal transverse energies, the emittance at the source can be written as [4] $\varepsilon_{\text{source}} = \sigma_y \sqrt{k_B T/2}$, where k_B is Boltmann's constant and T is the temperature of atoms in the MOT. The emittance at the target is approximately $\varepsilon_{\text{target}} = \sigma_{\text{target}} \left(\sigma_L / f\right) \sqrt{U}$, where σ_{target} is the rms size of the focal spot and σ_L is the rms size of the ion beam entering the focusing lens with focal length f. Using conservation of emittance, we equate the source and target emittances and solve for the rms spatial spread of the ion beam at the focus:

$$\sigma_{\text{target}} = \frac{\sigma_y}{\sigma_L} f \sqrt{\frac{k_B T}{2U}}. \quad (1)$$

Assuming parameters consistent with Fig. 3, $\sigma_y = 20$ μm, $\sigma_L = 53$ μm (one standard deviation of a uniformly illuminated 150 μm aperture), $f = 15$ mm, $T = 600$ μK, and $U = 1915$ V, we estimate that the 25% to 75% rise distance $d_{\text{target}} \approx 1.349 \times \sigma_{\text{target}} =$ 30 nm. Because the system incorporates a beam-defining aperture, the source emittance provides an overestimate of the target emittance, so we consider the above estimate to be an upper bound on the expected beam size.

Contributions to probe size from chromatic and spherical aberration (d_{chr} and d_{sph}, respectively) can be estimated and combined with source contribution d_{target} (estimated above) according to the formula [21]

$$d_{\mathrm{total}} = \sqrt{d_{\mathrm{chr}}^2 + (d_{\mathrm{sph}}^{1.3} + d_{\mathrm{target}}^{1.3})^{2/1.3}}. \quad (2)$$

We estimate these contributions to be $d_{\mathrm{chr}} < 8\,\mathrm{nm}$ and $d_{\mathrm{sph}} < 5\,\mathrm{nm}$, respectively, and as a result they account for less than 20 % of the observed rise distance of 26.7 nm.

To validate the dependence of Eq. (1) on MOT temperature T and beam energy U experimentally, we investigated the FIB size as a function of these parameters (Fig. 4). The temperature of the atoms in the MOT was varied by tuning the intensity of the MOT trapping laser beams. The energy of the beam was varied by scaling all of the accelerating voltages by the same factor. The aberration contributions d_{chr} and d_{sph} were the same for all data in Fig. 4. Furthermore, the accelerating voltages were tuned to reduce the emittance-lowering effect of the beam-defining aperture, thereby increasing the size of the source contribution relative to the aberrations. This emphasized the dependence of beam size on temperature and energy, and resulted in somewhat larger beam sizes than recorded in Fig. 3(c).

The measured rise distance vs. temperature data shown in Fig. 4(a) exhibit a monotonic increase as predicted by Eq. (1). The data were acquired at a beam energy of 1930 eV. The solid trend line is a fit to the probe size combination formula

$$d_{25/75} = \sqrt{d_{\mathrm{chr}}^2 + (d_{\mathrm{sph}}^{1.3} + AT^{1.3/2})^{2/1.3}}, \quad (3)$$

with d_{chr} and d_{sph} held fixed at 8 nm and 5 nm, respectively, and *A* treated as a free parameter in the fit. The agreement between the data and trend line shows consistency of the measurements with the expected scaling of the beam size with temperature.

The measured rise distance vs. beam energy data shown in Fig. 4(b) exhibit a monotonic decrease as expected from Eq. (1). The data were acquired at a temperature of 600 μK. The trend line in Fig. 4(b) is a fit to the expression

$$d_{25/75} = \sqrt{d_{\mathrm{chr}}^2 + (d_{\mathrm{sph}}^{1.3} + \frac{B}{U^{1.3/2}})^{2/1.3}}, \quad (4)$$

with d_{chr} and d_{sph} held fixed as with the temperature measurements and B as a free parameter. The rise distance data is consistent with the trend line at higher energies; however, at lower energies the data and trend line diverge. Coulomb interactions can increase beam emittance as the extraction electric field E (which is proportional to U in Fig. 4(b)) decreases [15]. Using the particle-tracking code developed in Ref. [15], we have simulated the Coulomb interactions for the experimental parameters relevant to Fig. 4(b). For $U = 1930$ eV, the simulations predict no significant increase in the emittance; however, at $U = 480$ eV, the simulations predict an emittance increase of up to 70 %. This behaviour is consistent with the observed deviation.

The measurements we present here demonstrate that it is possible to take advantage of the extremely low temperatures of laser-cooled atoms to realize a source of ions with both an emittance that is low enough and a current that is high enough to generate high quality secondary-electron images with nanoscale resolution. We look forward to enhanced performance of this ion source through several possible refinements of the technique. First, at higher beam energies, the achievable resolution will improve as seen from the trend in Fig. 4(b). Second, the chromatic contributions to the spot size, which are proportional to the beam energy spread, can be mitigated further by more tightly focusing the ionization laser. Third, further cooling of the atoms to lower temperatures is possible using a range of laser cooling techniques [22], which would result in even lower emittance. Fourth, faster loading of atoms into the MOT would increase beam current and brightness of the source [4,16]. Implementing these refinements would enable the formation of FIBs with performance exceeding that which is achievable with a LMIS over the range of energies typical for FIB applications. Furthermore, this technique can be used to create high resolution FIBs from a range of elements that are currently inaccessible by other methods.

We thank Mostafa Maazouz and Greg Schwind for helpful discussions and Alan Band, Steve Blankenship, Glenn Holland, Dustin Laur, and Dave Rutter for aid in the building the FIB platform.

REFERENCES

[1] Giannuzzi L A and Stevie F A 2005 *Introduction to focused ion beams: instrumentation, theory, techniques, and practice* (Springer)

[2] Orloff J, Swanson L and Utlaut M W 2003 *High resolution focused ion beams: FIB and its applications* (Springer)

[3] Chabala J M, Soni K K, Li J, Gavrilov K L and Levi-Setti R 1995 High-resolution chemical imaging with scanning ion probe SIMS *Int. J. Mass Spectrom.* **143** 191–212

[4] Hanssen J L, McClelland J J, Dakin E A and Jacka M 2006 Laser-cooled atoms as a focused ion-beam source *Phys. Rev. A* **74** 063416

[5] Ward B W, Notte J A and Economou N P 2006 Helium ion microscope: A new tool for nanoscale microscopy and metrology *J. Vac. Sci. Technol. B* **24** 2871

[6] Smith N S, Skoczylas W P, Kellogg S M, Kinion D E, Tesch P P, Sutherland O, Aanesland A and Boswell R W 2006 High brightness inductively coupled plasma source for high current focused ion beam applications *J. Vac. Sci. Technol. B* **24** 2902

[7] Steele A V, Knuffman B, McClelland J J and Orloff J 2010 Focused chromium ion beam *J. Vac. Sci. Technol. B* **28** C6F1

[8] Castaldo V, Hagen C W, Rieger B and Kruit P 2008 Sputtering limits versus signal-to-noise limits in the observation of Sn balls in a Ga+ microscope *J. Vac. Sci. Technol. B* **26** 2107

[9] Williams P, Lewis R K, Evans C A and Hanley P R 1977 Evaluation of a cesium primary ion source on an ion microprobe mass spectrometer *Anal. Chem.* **49** 1399–403

[10] Narum D H and Pease R F W 1988 Applications of a variable energy focused ion beam system *J. Vac. Sci. Technol. B* **6** 2115

[11] Freinkman B G, Eletskii A and Zaitsev S I 2004 A proposed laser source of ions for nanotechnology *Microelectronic Engineering* **73-74** 139–43

[12] Claessens B J, Reijnders M P, Taban G, Luiten O J and Vredenbregt E J D 2007 Cold electron and ion beams generated from trapped atoms *Phys. Plasmas* **14** 093101

[13] Hanssen J L, Hill S B, Orloff J and McClelland J J 2008 Magneto-Optical-Trap-Based, High Brightness Ion Source for Use as a Nanoscale Probe *Nano Lett.* **8** 2844–50

[14] Reijnders M, van Kruisbergen P, Taban G, van der Geer S, Mutsaers P, Vredenbregt E and Luiten O 2009 Low-Energy-Spread Ion Bunches from a Trapped Atomic Gas *Phys. Rev. Lett.* **102** 034802

[15] Steele A V, Knuffman B and McClelland J J 2011 Inter-ion coulomb interactions in a magneto-optical trap ion source *J. Appl. Phys.* **109** 104308

[16] van der Geer S B, Reijnders M P, de Loos M J, Vredenbregt E J D, Mutsaers P H A and Luiten O J 2007 Simulated performance of an ultracold ion source *J. Appl. Phys.* **102** 094312

[17] Wan W, Zhang Q, Cui Y and Wang E 2010 First principles study of lithium insertion in bulk silicon *J. Phys.: Condens. Matter* **22** 415501

[18] Niehus H, Heiland W and Taglauer E 1993 Low-energy ion scattering at surfaces *Surf. Sci. Rep.* **17** 213–303

[19] Schünemann U, Engler H, Zielonkowski M, Weidemüller M and Grimm R 1998 Magneto-optic trapping of lithium using semiconductor lasers *Opt. Commun.* **158** 263–72

[20] All uncertainties in this paper are intended to be interpreted as one-standard-deviation, combined standard uncertainty NIST Uncertainty Statement

[21] Barth J E and Kruit P 1996 Addition of different contributions to the charged particle probe size *Optik* **101** 101–9

[22] Metcalf H J and van der Straten P 1999 *Laser Cooling and Trapping* (New York: Springer)

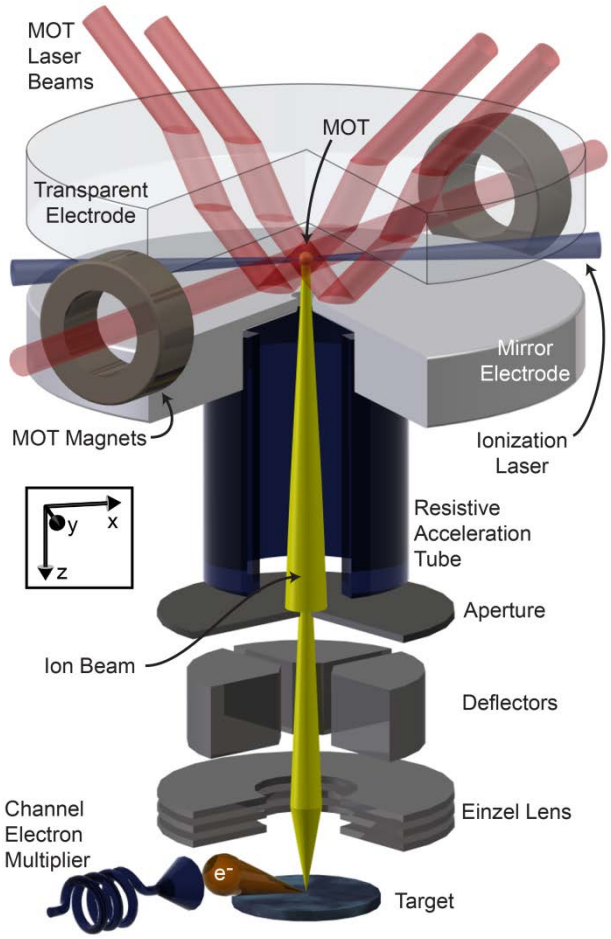

Fig. 1. Lithium focused ion beam system.

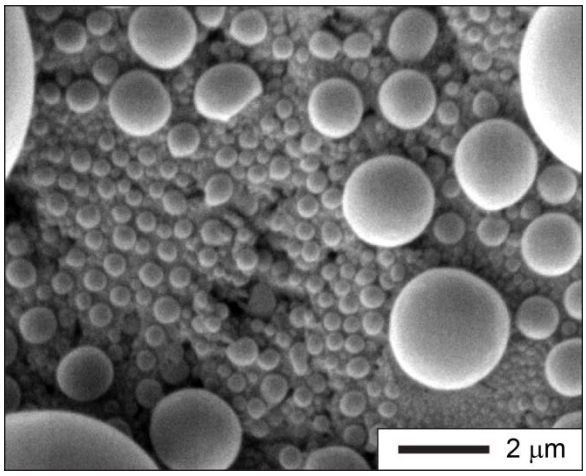

Fig. 2 Secondary electron image of tin spheres on carbon generated by a 2 keV lithium focused ion beam with 1 pA of probe current.

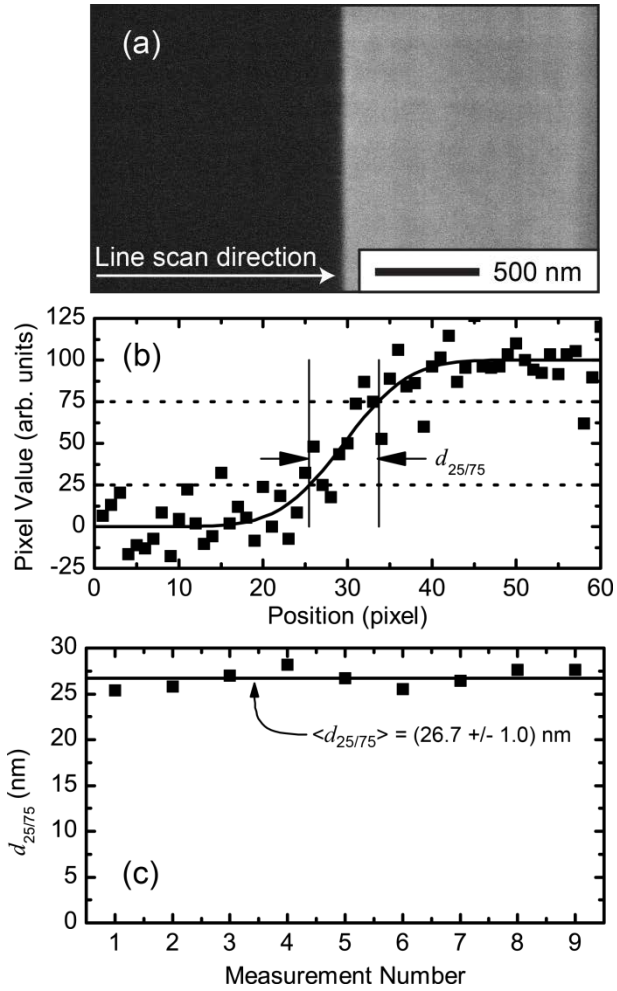

Fig. 3. (a) Secondary electron image of a cleaved silicon edge used for rise-distance profiling of a 2 keV lithium ion beam. (b) Sample rise distance measurement fit to a single line scan across the knife edge (1 pixel is 2.97 nm). (c) Repeated measurements of the rise distance under operating conditions yielding the best recorded beam size.

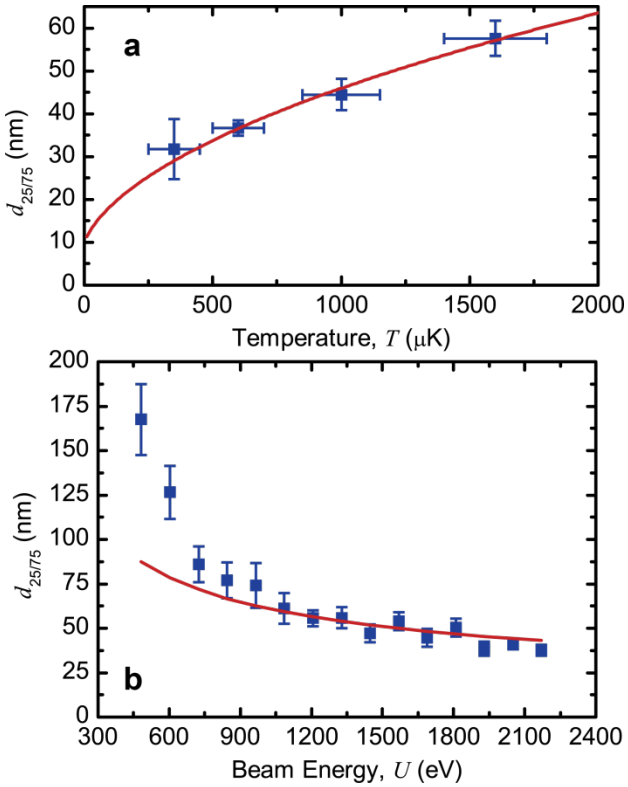

Fig. 4. Measured beam size (25 % to 75 % rise distance $d_{25/75}$) vs. (a) magneto-optical trap temperature *T* and (b) beam energy *U*. Error bars represent one-standard-deviation combined standard uncertainty. Solid lines are a fit to a probe size formula (see text).